Atomistic simulation of phonon heat transport across metallic vacuum nanogaps

Yangyu Guo,[1,*] Christophe Adessi,[1] Manuel Cobian,[2] and Samy Merabia[1,†]
[1]*Institut Lumière Matière, Université Claude Bernard Lyon 1-CNRS, Université de Lyon, Villeurbanne 69622, France*
[2]*Laboratoire de Tribologie et Dynamique des Systèmes, École Centrale de Lyon-CNRS, Université de Lyon, Ecully 69134, France*

(Received 25 May 2022; revised 15 July 2022; accepted 22 July 2022; published 3 August 2022)

The understanding and modeling of heat transport across nanometer and subnanometer gaps, where the distinction between thermal radiation and conduction becomes blurred, remains an open question. In this work, we present a three-dimensional atomistic simulation framework by combining the molecular dynamics (MD) and phonon nonequilibrium Green's function (NEGF) methods. The relaxed atomic configuration and interaction force constants of metallic vacuum nanogaps are generated from MD as inputs into harmonic phonon NEGF. Phonon tunneling across gold-gold and copper-copper nanogaps is quantified, and is shown to be a significant heat transport channel below a gap size of 1 nm. We demonstrate that lattice anharmonicity contributes to within 20%–30% of phonon tunneling depending on gap size, whereas electrostatic interactions turn out to have a weak effect for the small bias voltage typically used in experimental measurements. This work provides detailed information of the heat current spectrum and interprets the recent experimental determination of thermal conductance across gold-gold nanogaps. Our study contributes to deeper insight into heat transport in the extremely near-field regime, as well as hints for future experimental investigation.

DOI: 10.1103/PhysRevB.106.085403

I. INTRODUCTION

When the distance between two solid objects drops down to a few nanometers or even smaller, heat transport lies in the extremely near-field regime where the interplay of thermal radiation and conduction plays an important role [1,2]. Understanding extremely near-field heat transport is of vital importance in many applications including scanning tunneling microscopy [3,4], heat assisted magnetic recording [5,6], noncontact friction [7–9], thermal contact resistance [10,11], and so on. The two recent experimental reports of thermal conductance in this regime [12,13] are, however, controversial. Kloppstech *et al.* [12] observed giant thermal conductance of nanometer gaps while Cui *et al.* [13] found much smaller values below the detection limit of their probe. The underlying physical mechanism of heat transfer thus remains still an open question.

One possible mechanism to explain the giant experimental thermal conductance in the gold tip-surface nanogap [12] is the phonon tunneling across the nanogap. As two solid objects are sufficiently close to each other, the transfer of lattice vibration (phonons) may occur via the direct atomic interaction across the nanogap. There have been already some investigations of phonon tunneling across nanogaps by either harmonic or anharmonic theoretical approaches. The harmonic approaches were usually based on Landauer's formalism of quantum transport, with the phonon transmission obtained through various methods: (i) phonon nonequilibrium Green's function (NEGF) formalism [14–18], (ii) elastic continuum model [19–22], or (iii) harmonic lattice dynamics [23,24]. Recently there has also been a fluctuational electrodynamic model for acoustic phonon tunneling across the vacuum gap in the elastic continuum limit [25,26]. The harmonic phonon NEGF simulations were mostly based on simplified one-dimensional (1D) formalism except in the very recent first-principles modeling of phonon transport across a Si-Si nanogap [18]. In addition, the nanogap configuration was usually not relaxed in both harmonic phonon NEGF and lattice dynamic methods except in the first-principles study [18]. The lattice anharmonicity was instead included in the recent molecular dynamics (MD) simulation of heat transport across Pt-Pt nanogaps [27]. However, the anharmonic effect on the thermal conductance of the nanogap has not yet been elucidated.

In this work, we present an atomistic modeling of phonon heat transport across metallic nanogaps by combining MD simulation and three-dimensional (3D) phonon NEGF formalism. The relaxed nanogap configuration and atomic interaction forces are generated from MD as inputs into the phonon NEGF. Furthermore, we extract and compare the spectral thermal conductance across the nanogap from both methods. Thus we provide a robust computational framework to investigate the effects of anharmonicity and electrostatics. The remainder of the paper is organized as follows. The atomistic simulation methodology will be introduced in Sec. II, and the results and discussions are given in Sec. III, with the concluding remarks finally made in Sec. IV.

II. METHODOLOGY

We model the phonon heat transport across a fcc (face-centered cubic) metal-metal nanogap, as shown in Fig. 1(a). Our atomistic simulation framework combines both the classical MD [28,29] and phonon NEGF methods [30,31]. The MD

---

[*] yangyuhguo@gmail.com
[†] samy.merabia@univ-lyon1.fr

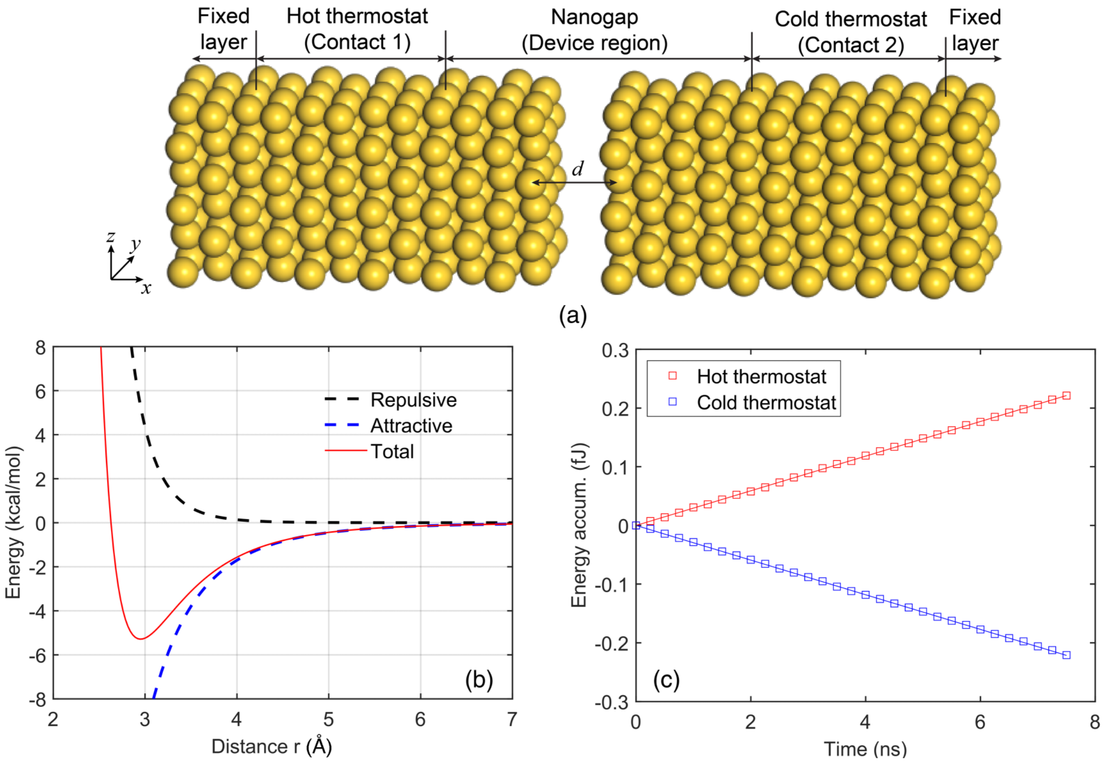

FIG. 1. Atomistic simulation of phonon heat transport across a metallic nanogap: (a) schematic of the Au-Au nanogap with a gap size d and periodic cross section; (b) Lennard-Jones potential for interaction between Au atoms; (c) energy accumulations at the hot and cold thermostats in MD (molecular dynamics) simulation of the Au-Au gap with $d = 3.94$ Å at 300 K; the discrete points represent the MD data while the solid lines are linear fitting.

includes all the order of anharmonicity automatically, whereas the harmonic phonon NEGF is adopted in this work due to too large computational cost of the anharmonic formalism [32]. The same empirical atomic interaction potential is employed in MD and NEGF, as will be explained later.

A. Molecular dynamics simulation

The classical NEMD (nonequilibrium MD) simulation is implemented in the open-source package LAMMPS [33]. We consider two types of metallic nanogaps: Au-Au and Cu-Cu gaps. The goal of our study on the Au-Au nanogap is to explain the recent experimental data of thermal conductance between the gold tip and gold substrate [12,13]. The Cu-Cu nanogap is also considered to investigate the effect of anharmonicity since copper is less anharmonic than Au based on the value of the Grüneisen parameter [34]. The 12-6 Lennard-Jones pairwise potential is adopted as seen in Fig. 1(b), with the parameters for Au and Cu detailed in Ref. [35], which provide a good description of the surface and interface properties relevant to the situation in the present study. The cutoff radius in MD simulation is 12 Å for both metals, which is large enough to include the long-range atomic interaction [35]. We have also checked that the long-range interaction between metallic atoms is indeed captured in the Lennard-Jones potential by comparing to the Grimme's density functional dispersion correction [36], as detailed in Appendix A. The parallel plate-plate configuration is considered as shown in Fig. 1(a), where periodic boundary conditions are used in the transverse direction. A very large cross section of 16 uc × 16 uc is adopted for both Au and Cu gaps after careful independence verification. Here 1 uc denotes one cubic conventional unit cell of fcc metals with four atoms. In the transport direction, we have sandwiched the nanogap between hot and cold thermostats with the same length of 4 uc. Two fixed layers with the same length of 2 uc are imposed on both ends of the system. The number of atomic unit cells in the nanogap region are 6 and 7, respectively, for the Au gap and the Cu gap, which are equally divided into both sides. These numbers are large enough to ensure that there is no direct interaction between one side of the nanogap and the thermostat on the other side. The gap size (d) is defined as the distance between the centers of the two surface atomic layers adjacent to the gap.

During the MD simulation, a time step of 0.5 fs is used. For both metal cases, firstly 1 000 000 time steps (0.5 ns) are run to relax the whole system under the *NPT* (isothermal-isobaric) ensemble. Then the fixed layers on both ends are fixed and 4 000 000 time steps (2 ns) are run to make the free part reach a steady state under the effect of Langevin thermostats in the *NVE* (microcanonical) ensemble. Finally, 15 000 000 time steps (7.5 ns) of steady-state runs are done for the calculation and analysis of the gap thermal conductance. To avoid the collapse of the gap structure due to the attractive interatomic force, a uniform tethering is exerted by attaching a harmonic spring (only along the transport direction) to each atom within the surface atomic monolayers adjacent to the nanogap. The spring stiffness is low in order to not perturb the phonon dynamics too much, as to be discussed later. The thermal conductance of the nanogap is extracted based on the energy accumulation at the hot and cold thermostats, as exemplified in Fig. 1(c) for the Au-Au gap with $d = 3.94$ Å at 300 K.

The frequency-dependent thermal conductance (or the spectral thermal conductance) is obtained by a spectral heat current (SHC) decomposition scheme [37,38], where the total heat current Q is written as

$$Q = \int_0^\infty q(\omega)\frac{d\omega}{2\pi} = \sum_{\substack{i\in I\\ j\in J}} \int_0^\infty q_{i\to j}(\omega)\frac{d\omega}{2\pi}, \tag{1}$$

where ω is the angular frequency of phonons; I, J denote separately the left and right sides of the nanogap region. The SHC between atom i and atom j is calculated by $q_{i\to j}(\omega) = 2\mathrm{Re}[\tilde{K}_{ji}(\omega)]$, where "Re" denotes the real part and $\tilde{K}_{ji}(\omega)$ is the Fourier transform of the atomic force-velocity correlation function between two time instants t_1 and t_2 [37,38]:

$$K_{ji}(t_1 - t_2) = \tfrac{1}{2}\langle \mathbf{F}_{ji}(t_1)\cdot[\mathbf{v}_j(t_2) + \mathbf{v}_i(t_2)]\rangle. \tag{2}$$

In Eq. (2), $\mathbf{F}_{ji}$ denotes the force acting on atom j due to atom i, and $\mathbf{v}_i$ and $\mathbf{v}_j$ are the atomic velocities. The brackets "$\langle\rangle$" in Eq. (2) denote the ensemble average, which is calculated through time average in MD simulation. Following previous work, we consider only harmonic terms in $\mathbf{F}_{ji}$ such that the calculation of the SHC is simplified [38]:

$$q_{i\to j}(\omega) = -\frac{2}{t_{\mathrm{simul}}\omega}\sum_{\alpha,\beta}\mathrm{Im}\left[\hat{v}_i^{\alpha}(\omega)^{*}\Phi_{ij}^{\alpha\beta}\hat{v}_j^{\beta}(\omega)\right], \tag{3}$$

where $\hat{v}_i^{\alpha}(\omega)$, $\hat{v}_j^{\beta}(\omega)$ are the Fourier transforms of the atomic velocities along the α, β directions, respectively, with "*" denoting the complex conjugate. $\Phi_{ij}^{\alpha\beta}$ is the harmonic (second-order) force constant matrix, "Im" denotes the imaginary part, and t_{simul} is the sampling simulation time. Note that the lattice anharmonicity is still included in the atomic velocity statistics in Eq. (3). In practical implementation, we output the time-dependent atomic velocities during the aforementioned 7.5 ns steady-state runs. The harmonic force constant matrix is computed based on the relaxed gap configuration obtained in the equilibration stage. The spectral thermal conductance per unit area is finally obtained as $h_\omega = q(\omega)/(2\pi A_c\Delta T)$, with A_c and ΔT the cross-sectional area and the temperature difference between thermostats, respectively. The thermal conductance of the nanogap can also be obtained by integrating the SHC from NEMD, which is usually close to that by the direct NEMD except in the presence of very strong anharmonicity. The direct NEMD result of the thermal conductance is used for discussion throughout this work unless stated otherwise.

B. Nonequilibrium Green's function method

In parallel, the harmonic phonon NEGF formalism is adopted in this work, with the retarded Green's function calculated in matrix notation as [39,40]

$$\mathbf{G}^{\mathrm{R}}(\omega;\mathbf{q}_\perp) = [\omega^2\mathbf{I} - \tilde{\mathbf{\Phi}}(\mathbf{q}_\perp) - \mathbf{\Sigma}^{\mathrm{R}}(\omega;\mathbf{q}_\perp)]^{-1}, \tag{4}$$

where the superscript "–1" means the inverse of a matrix; $(\omega, \mathbf{q}_\perp)$ denote the frequency and wave-vector dependences along the transport direction and transverse periodic direction, separately; $\mathbf{I}$ is the unity matrix; and $\tilde{\mathbf{\Phi}}(\mathbf{q}_\perp)$ is the Fourier's representation of the harmonic dynamic matrix [32,39]. The retarded self-energy matrix includes the contribution only from the two contacts, $\mathbf{\Sigma}^{\mathrm{R}}(\omega;\mathbf{q}_\perp) = \mathbf{\Sigma}_1^{\mathrm{R}}(\omega;\mathbf{q}_\perp) + \mathbf{\Sigma}_2^{\mathrm{R}}(\omega;\mathbf{q}_\perp)$, which are related to the surface Green's functions of contact 1 and contact 2 as calculated by the decimation technique [41].

Once the retarded Green's function is obtained, the phonon transmission through the nanogap is calculated by [39,40]

$$\Xi(\omega) = \frac{1}{N}\sum_{\mathbf{q}_\perp}\mathrm{Tr}[\mathbf{\Gamma}_1(\omega;\mathbf{q}_\perp)\mathbf{G}^{\mathrm{R}}(\omega;\mathbf{q}_\perp)\mathbf{\Gamma}_2(\omega;\mathbf{q}_\perp)\mathbf{G}^{\mathrm{A}}(\omega;\mathbf{q}_\perp)], \tag{5}$$

where N denotes the total number of discrete transverse wave vectors ($\mathbf{q}_\perp$); "Tr" denotes the trace of a matrix; $\mathbf{G}^{\mathrm{A}}$ the advanced Green's function as the Hermitian conjugate of $\mathbf{G}^{\mathrm{R}}$; and the broadening matrices of contacts 1 and 2, $\mathbf{\Gamma}_{1(2)} = i[\mathbf{\Sigma}_{1(2)}^{\mathrm{R}} - \mathbf{\Sigma}_{1(2)}^{\mathrm{A}}]$, with $i = \sqrt{-1}$ here and $\mathbf{\Sigma}^{\mathrm{A}}$ the advanced self-energy matrix as the Hermitian conjugate of $\mathbf{\Sigma}^{\mathrm{R}}$. The thermal conductance per unit area is related to the transmission based on the Landauer's formula [30,31,39]:

$$h = \frac{1}{A_c}\int_0^\infty \hbar\omega\frac{\partial f_{\mathrm{BE}}(\omega)}{\partial T}\,\Xi(\omega)\frac{d\omega}{2\pi}, \tag{6}$$

where $\hbar$ is the reduced Planck constant, and $f_{\mathrm{BE}}(\omega)$ is the Bose-Einstein distribution of phonons. To have a direct comparison to the MD simulation, the classical limit of Eq. (6) is written as follows by replacing the quantum heat capacity $[\hbar\omega\partial f_{\mathrm{BE}}(\omega)/\partial T]$ by the classical one (k_B):

$$h = \frac{1}{A_c}\int_0^\infty k_B\,\Xi(\omega)\frac{d\omega}{2\pi}, \tag{7}$$

where k_B is the Boltzmann constant.

As we aim to compare the phonon NEGF and MD results, the effect of tethering of the surface atomic monolayers adjacent to the nanogap in MD simulation must also be considered in the phonon NEGF method. To do that, a diagonal term is added into the dynamic Eq. (4) of the retarded Green's function:

$$\mathbf{G}^{\mathrm{R}}(\omega;\mathbf{q}_\perp) = \left[\omega^2\mathbf{I} - \tilde{\mathbf{\Phi}}(\mathbf{q}_\perp) - \frac{k_{\mathrm{spring}}}{m}\mathbf{I}_1 - \mathbf{\Sigma}^{\mathrm{R}}(\omega;\mathbf{q}_\perp)\right]^{-1}, \tag{8}$$

where $\mathbf{I}_1$ is a diagonal matrix with diagonal components [1 0 0] associated with each atom under the tethering along only the transport direction (x direction), and k_{spring} the spring constant of the harmonic spring and m the atomic mass. Equation (8) is derived based on the lattice dynamic equation with an external tethering force; more details are given in Appendix B.

The required inputs into phonon NEGF include the atomic configuration of the nanogap and the harmonic force constant matrix, both of which are generated from MD simulation. A simulation cell with a cross section of 1 uc × 1 uc is extracted from the cross-sectional center of the relaxed nanogap in the aforementioned equilibration stage. The length of the simulation cell for phonon NEGF is the same as that in MD simulation. We have checked that the transverse lattice symmetry is well preserved in the nanogap to justify the Fourier's

TABLE I. The initial and relaxed Au-Au nanogap configurations under the corresponding tethering spring of surface atomic layers adjacent to the gap in molecular dynamics simulation.

d_{init} (Å)	k_{spring} (N/m)	f_{spring} (THz)	d_{relax} (Å)
4.5	16.68	1.14	3.94
5.0	9.73	0.87	4.43
5.5	5.56	0.66	4.92
6.0	4.17	0.57	5.56
7.0	0.70	0.23	6.28

representation with such a cross-section period in phonon NEGF. The harmonic force constant matrix of the nanogap is computed by combining LAMMPS with the same Lennard-Jones potential and the open-source package PHONOPY [42] based on the finite-displacement method. The phonon NEGF simulation is implemented in our highly parallelized computational framework [32], with a very dense transverse wave vector of 100 × 100 after independence verification.

C. Configurations of nanogaps

In our NEMD simulation, the nanogaps will collapse in the natural state due to surface attraction. In the realistic situation of a tip-surface system, the tip is stretched as it approaches the surface due to attractive, adhesive forces between the tip and surface, as clearly shown in a previous experimental study [3]. We exert a tethering force on the surface atomic layers adjacent to the nanogap to avoid the instability owing to structure relaxation. On the other hand, to minimize the influence of the tethering on the atomic and phonon dynamics around the nanogap, we use a tethering force as small as possible. In practical implementation, we construct a nanogap with an initial gap size d_{init}, and run *NPT* equilibrations under a series of decreasing tethering spring constants. We adopt the value of the tethering spring constant just before the collapse of the nanogap. The relaxed gap size d_{relax} under the adopted tethering is slightly smaller than the initial value (d_{init}). Several nanogaps are considered, with their initial (final) relaxed gap sizes and the corresponding tethering spring constants given in Tables I and II for Au and Cu cases, separately. Also we define the tethering spring frequency as $\omega_{\text{spring}} \equiv 2\pi f_{\text{spring}} = \sqrt{k_{\text{spring}}/m}$, which will be compared to the dominant frequency of phonons tunneled across the nanogap in later discussions.

Although the tethering is unavoidable, we will show that it does not perturb too much the phonon dynamics across the nanogap, especially at larger gap sizes. As the global variation of thermal conductance with nanogap size is much larger (several orders of magnitude), the tethering will not impact the general trend and final conclusion. Similar system collapse has been reported in a previous MD simulation of near-field heat transport between two silica nanoparticles, where the authors stopped the simulation after a 10% reduction of the initial interparticle distance [43]. Even though the stability issue was not explained in the recent MD study of heat transport across the Pt-Pt nanogap [27], we believe the situation should be similar as the soft Lennard-Jones potential was also adopted.

TABLE II. The initial and relaxed Cu-Cu nanogap configurations under the corresponding tethering spring of surface atomic layers adjacent to the gap in molecular dynamics simulation.

d_{init} (Å)	k_{spring} (N/m)	f_{spring} (THz)	d_{relax} (Å)
4.0	18.07	2.08	3.45
4.5	11.12	1.63	4.05
5.0	6.95	1.29	4.62
5.5	4.17	1.00	5.12
6.0	2.78	0.82	5.67

D. Electronic tunneling heat transport

The electrons will tunnel across the metallic nanogap with a gap size below 1 nm [12,13] and also contribute to heat transport. For comparison, we estimate this electronic tunneling heat current leaving contact 1 based on the following formula:

$$Q_{e1} = \int_0^\infty (E_x - \mu_1)[N_1(E_x) - N_2(E_x)]\tau(E_x)\mathrm{d}E_x + \int_0^\infty \mathrm{d}E_x \tau(E_x)\frac{m}{2\pi^2\hbar^3}\int_0^\infty \mathrm{d}E_r[f_1(E) - f_2(E)]E_r, \tag{9}$$

where E_x and $\tau(E_x)$ represent, respectively, the energy and the transmission probability of electrons along the transport direction, E_r being the electron energy along the transverse direction in the cylindrical coordinate, and the total electron energy $E = E_x + E_r$. The chemical potentials of electrons in the two metallic contacts are denoted by μ_1 and μ_2, respectively. The expressions of electron number distribution along the transport direction $N_{1(2)}(E_x)$ and Fermi-Dirac distribution $f_{1(2)}(E)$ in contacts are detailed in Appendix C, where the derivation of Eq. (9) is also shown. The present formulation is improved over the previous one in Ref. [17] in two aspects: (i) subtraction of the chemical potential in defining the heat current in contrast to an energy current in previous work; (ii) a more accurate account for the transverse kinetic energy (E_r) in contrast to an approximation (k_BT) in previous work.

III. RESULTS AND DISCUSSIONS

In this section, we present the results of overall and spectral thermal conductance across the nanogaps by comparing the NEMD simulation and phonon NEGF modeling in Sec. III A. Then the effect of anharmonicity is investigated through the temperature-dependent results in Sec. III B. Finally the effect of electrostatics and the explanation of experimental data are discussed in Secs. III C and III D, respectively.

A. Overall and spectral thermal conductance

1. Thermal conductance

The gap size dependent thermal conductances of the Au-Au and Cu-Cu nanogaps at room temperature (300 K) by NEMD and phonon NEGF are shown in Figs. 2(a) and 2(b), respectively. In NEMD, we use a temperature difference of ±50 K (i.e., 100 K), which is sufficiently small to remain in

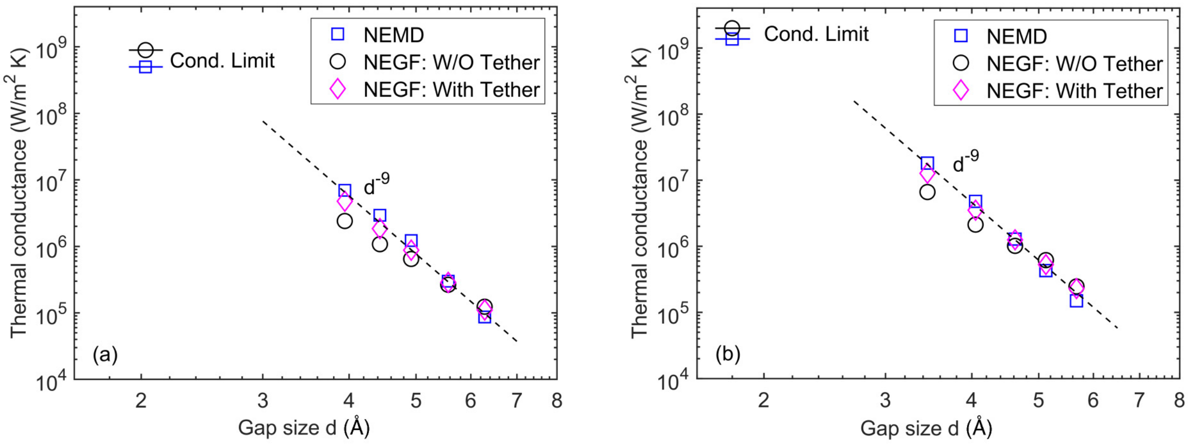

FIG. 2. Thermal conductance versus gap size at room temperature (300 K): (a) Au-Au gap, (b) Cu-Cu gap. The blue squares denote the direct NEMD (nonequilibrium molecular dynamics) result; the magenta diamonds and the black circles represent the phonon NEGF (nonequilibrium Green's function) results with and without tethering of the surface atomic layers adjacent to the nanogap. The dashed line represents a power-law scaling of d^{-9}. The conduction limit (Cond. Limit) corresponds to the contact situation (with a gap size of half the lattice constant).

the linear regime while it is sufficiently large to have good statistics due to the very weak interaction across the nanogap. For both cases, we do not consider gap size larger than ~7 Å as the heat transport is too weak to obtain statistically meaningful heat currents in NEMD. On the other hand, we do not consider too small a gap size as the nanogap is prone to collapse. In all, the nanogap size lies in a range where the atomic interaction is dominated by the attractive long-range dispersion force in Fig. 1(b). The NEMD thermal conductance of the nanogap decreases very rapidly with increasing gap size (d), following approximately a power law of d^{-9}. The usual NEGF conductance based on Eq. (4) is appreciably lower than the NEMD one at small gap size, which is mainly due to the perturbation stemming from the tethering treatment in NEMD. With the correction of the tethering force in Eq. (8), the NEGF conductance generally agrees with the NEMD one in the considered range of gap size. This also indicates the weak effect of anharmonicity at room temperature.

We now compare the calculated thermal conductance of the Au-Au nanogap to the recent experimental results [12,13]. As the parallel plate-plate configuration is considered in our simulations, its thermal conductance per unit area (h) [W/m^2 K] is converted into the thermal conductance (G) [W/K] of a tip-plate configuration in experimental setup using the classical Derjaguin approximation [17,22]:

$$G(\tilde{d}) = \int_0^{r_{\text{tip}}} h(d) 2\pi r \mathrm{d}r, \tag{10}$$

where r_{tip} is the radius of the tip, and r is the radius of a horizontal slice of the tip with a distance d to the plate, with $d = \tilde{d} + r_{\text{tip}} - \sqrt{r_{\text{tip}}^2 - r^2}$, $\tilde{d}$ being the distance between the tip apex and the plate. Since the phonon thermal conductance $h(d)$ decreases very rapidly with d, the relevant gap size for the integration in Eq. (10) is much smaller than the tip radius in the experimental setup ($r_{\text{tip}} = 30$ nm [12] and $r_{\text{tip}} = 150$ nm [13]), such that $r_{\text{tip}} \gg d - \tilde{d}$ and we have, approximately, $r^2 \approx 2r_{\text{tip}}(d - \tilde{d})$. Introducing $\tilde{d}' = (d - \tilde{d})$, we have $r^2 \approx 2r_{\text{tip}}\tilde{d}'$ and Eq. (10) is simplified to

$$G(\tilde{d}) = 2\pi r_{\text{tip}} \int_0^{\frac{r_{\text{tip}}}{2}} h(\tilde{d}' + \tilde{d}) \mathrm{d}\tilde{d}'. \tag{11}$$

In practical implementation, we consider the tip-plate gap size ($\tilde{d}$) up to 6 Å with the upper limit of the integration in Eq. (11) adopted as $\tilde{d}' = (9\text{ Å} - \tilde{d})$. This ensures the accuracy as the integrand h at the upper limit ($d = 9$ Å) is at least two orders of magnitude smaller than the value at the lower limit ($d = \tilde{d} \leqslant 6$ Å), as shown in Fig. 3(a). As the NEGF result with tethering correction is very close to the NEMD one, we adopt the former as the thermal conductance of the plate-plate configuration. An analytical expression is obtained through a fitting of the phonon NEGF data in Fig. 3(a), and then used for the integration in Eq. (11). For nanogap size (d) larger than those in Table I, we follow the same procedure to generate the nanogap configuration and atomic interaction forces from MD as inputs into phonon NEGF.

In Fig. 3(a), the thermal conductance by the 1D phonon NEGF with Lennard-Jones potential [17] also is included, which shows almost the same power-law scaling yet much larger magnitude compared to the present 3D NEGF. The underlying reason is that the average phonon group speed along different directions in 3D angular space is much smaller than that along the monodirection in the simplified 1D space [17]. This demonstrates the necessity of 3D atomistic simulation to accurately describe the phonon transport across vacuum nanogaps. The thermal conductance by the 3D harmonic lattice dynamic model [24] is higher than the present NEGF result, as shown in Fig. 3(a). Such difference could be mainly caused by the different treatments of atomic interaction, as the *ab initio* force constant and a Lennard-Jones potential are adopted, respectively, in the contacts and across the vacuum gap in Ref. [24]. We also include in Fig. 3(a) the result by the elastic continuum model [25], which is generally a few orders of magnitude smaller than various atomistic modeling results. Especially in the conduction limit ($d \sim 2$ Å), the continuum model predicts a thermal conductance

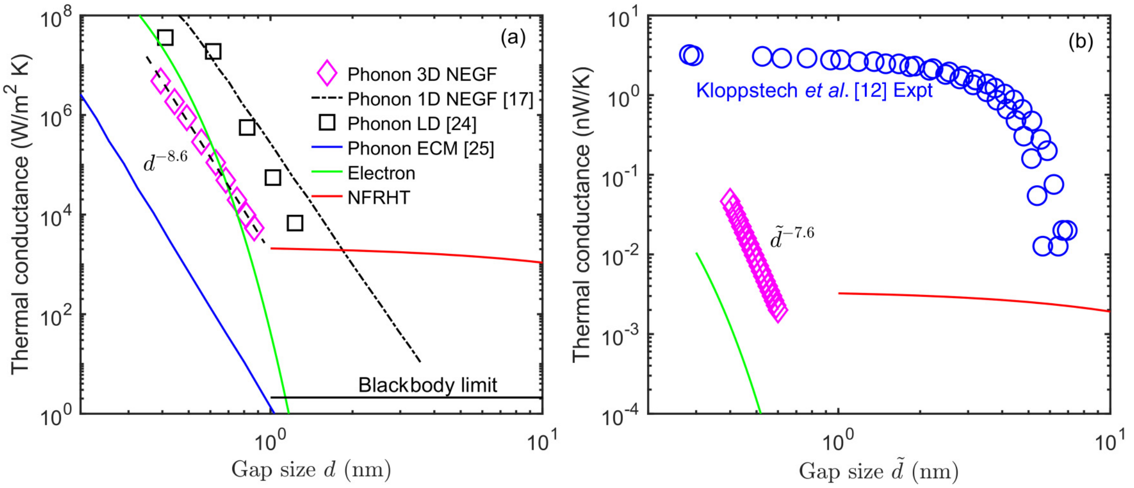

FIG. 3. Thermal conductance versus gap size around room temperature: (a) plate-plate configuration, (b) tip-plate configuration corresponding to experimental setup. The magenta diamonds denote the present 3D phonon NEGF (nonequilibrium Green's function) result with tethering of the surface atomic layers adjacent to the nanogap, the black dash-dotted line represents the 1D phonon NEGF result from Ref. [17], the black squares denote the lattice dynamic (LD) model result of phonons from Ref. [24], the blue solid line denotes the elastic continuum model (ECM) result of phonons from Ref. [25], the red solid line denotes the NFRHT (near-field radiative heat transfer) result predicted by the fluctuational electrodynamic theory, and the green solid line denotes the contribution of electron tunneling to heat transport, whereas the blue circles represent the experimental data [12].

of $\sim 10^6$ W/m^2 K, which is around three orders of magnitude smaller than the present atomistic modeling result ($\sim 10^9$ W/m^2 K). A clear understanding of the underlying reason remains an open question in the current stage due to very different frameworks. From our perspective, the different orders of magnitude of phonon thermal conductance mainly come from: (i) the different descriptions of interfacial phonon scattering, i.e., continuum versus atomistic; (ii) the different treatments of van der Waals force. In particular, only surface-surface interactions across the nanogap are taken into account in the continuum model, whereas the cross-gap interaction between atoms within a cutoff range near the surfaces is also considered in the atomistic modeling.

The phonon thermal conductance of the gold tip-plate nanogap with a tip radius of $r_{\text{tip}} = 30$ nm [12] is shown in Fig. 3(b), with a power-law scaling of $G \propto \tilde{d}^{-7.6}$. For comparison, we also include the electronic thermal conductance and the near-field radiative heat transfer (NFRHT) result by the fluctuational electrodynamic theory [44] using the local dielectric function of gold [45]. The NFRHT thermal conductance is calculated for nanogap size only down to 1 nm, below which the nonlocal effect will play a significant role and saturate the conductance [46]. The Derjaguin approximation in Eq. (10) is also valid for NFRHT, while it is not valid for electronic tunneling. We follow an approximate scheme for electron tunneling proposed in Ref. [22]: $G(\tilde{d}) = h(d = \tilde{d})\pi r_{\text{Au}}^2$, with $r_{\text{Au}} = 1.35$ Å the radius of a gold atom. As shown in Fig. 3(b), the phonon thermal conductance is dominant over the photon and electron counterparts in this extremely near-field regime. However, the phonon thermal conductance is still much smaller than the experimental data of Kloppstech *et al.* [12]. With the tip radius of $r_{\text{tip}} = 150$ nm [13], we obtain a maximal phonon thermal conductance of 0.23 nW/K at the minimal $\tilde{d} = 4$ Å for the tip-plate configuration. This conductance is of the same order of magnitude as the measured maximal possible thermal conductance ($\sim$0.5 nW/K) of the smallest gaps after a careful cleaning process [13]. The thermal conductance at larger gap size is indeed below the detection limit of their probe, as consistent with the conclusion drawn in the experiment of Cui *et al.* [13]. Further discussion about the explanation of the giant thermal conductance in the experiment of Kloppstech *et al.* [12] is given in Sec. III D.

2. *Spectral thermal conductance*

The spectral thermal conductances of Au-Au nanogaps are extracted from NEMD simulations based on Eqs. (1)–(3), as shown in Fig. 4(a). The phonon heat current spectrum is reduced very sharply beyond a critical frequency ($\sim$2 THz) as the higher-frequency phonons are more difficult to tunnel across the nanogap. Here the critical frequency denotes a frequency beyond which the phonon transmission drops rapidly. With the increase of nanogap size from 3.94 to 6.28 Å, the spectral thermal conductance decreases about two orders of magnitude, which explains well the rapid decay of thermal conductance in Fig. 2(a). Such rapid decay of phonon tunneling with gap size is related to the r^{-6} distance-dependent dispersion force of the Lennard-Jones potential. We also include the usual NEGF spectral conductance in Fig. 4(a), which shows good consistency with the NEMD result at high frequency while there is appreciable deviation at low frequency for the 3.94 and 4.92 Å nanogaps. The frequency range with large deviation is around the tethering spring frequency in Table I, evidencing more definitely that the difference between the thermal conductances by NEGF and by NEMD at small gap size in Fig. 2(a) is relevant to the perturbation introduced by tethering in NEMD. The restoration of the tethering spring to balance the collapse trend impacts the surface lattice

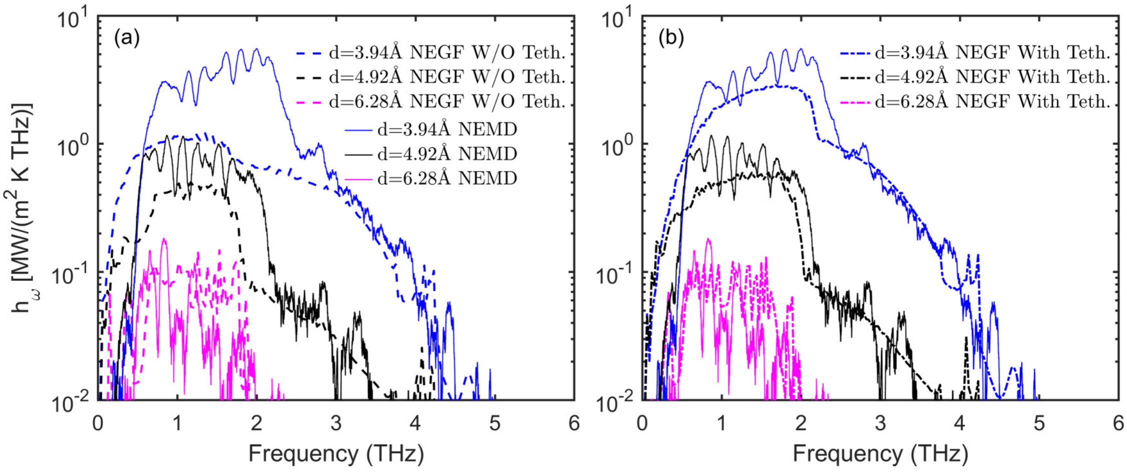

FIG. 4. Spectral thermal conductance of Au-Au nanogaps at room temperature (300 K): NEMD result versus NEGF results (a) without and (b) with tethering of the surface atomic layers adjacent to the nanogap. The solid lines represent the NEMD (nonequilibrium molecular dynamics) results, whereas the dashed and dash-dotted lines represent the phonon NEGF (nonequilibrium Green's function) results without and with tethering, respectively.

vibration at similar frequency (i.e., close to the tethering spring frequency). At smaller gap size, the nanogap is more prone to collapse which corresponds to stronger surface-surface interaction and stiffer tethering spring to avoid instability. This explains the shift of the frequency range with appreciable deviation to lower value with increasing nanogap size in Fig. 4(a). With the tethering correction, the NEGF results of spectral thermal conductance show general agreement with the NEMD ones, as illustrated in Fig. 4(b). There is still some deviation around the tethering spring frequency, due to the fact that only the harmonic interaction is taken into account in NEGF.

The results of Cu-Cu nanogaps are similar as shown in Fig. 5. The critical frequency beyond which the phonon heat current spectrum is reduced sharply is almost twice (∼4 THz) the value for the Au-Au nanogaps, as the atomic mass of Au is close to 3–4 times that of Cu. With the tethering correction, the deviation between NEGF and NEMD results around the tethering spring frequency is apparently smaller than that in Au-Au nanogaps. This could be explained by the weaker anharmonicity of Cu as compared to Au based on the average Grüneisen parameters of 2.0 and 3.0, respectively [34]. In addition, the spectral thermal conductance profile of the Cu nanogap is more peaky than that of the Au nanogap because of large fluctuations due to both smaller atomic mass and the weak nature of atomic interaction across the nanogap.

B. Effect of anharmonicity

Anharmonic effects are known to play a non-negligible role in interfacial heat transfer [37,47] but remain ambiguous in heat transport across nanogaps. The present atomistic simulation framework provides a unique tool to uncover the role of anharmonicity through a comparison of the results of NEMD

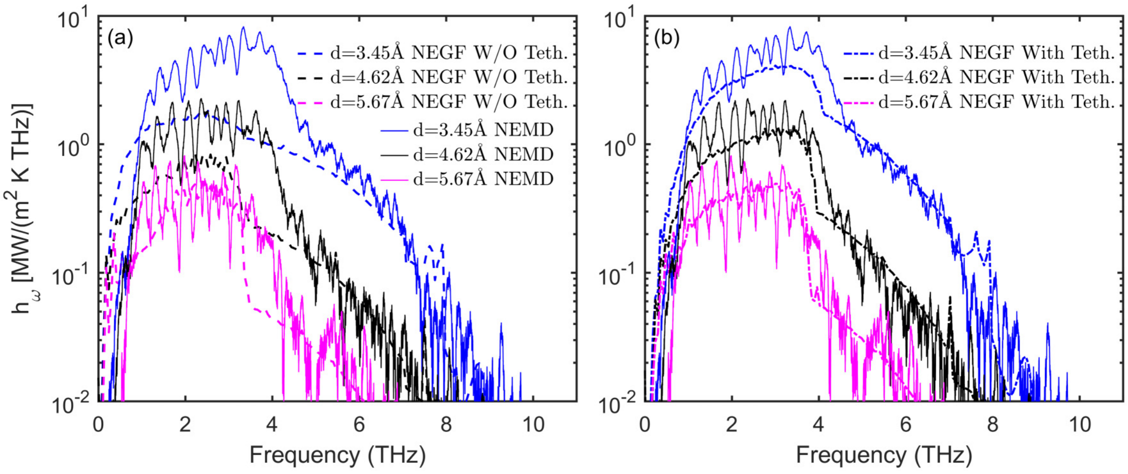

FIG. 5. Spectral thermal conductance of Cu-Cu nanogaps at room temperature (300 K): NEMD result versus NEGF results (a) without and (b) with tethering of the surface atomic layers adjacent to the nanogap. The solid lines represent the NEMD (nonequilibrium molecular dynamics) results, whereas the dashed and dash-dotted lines represent the phonon NEGF (nonequilibrium Green's function) results without and with tethering, respectively.

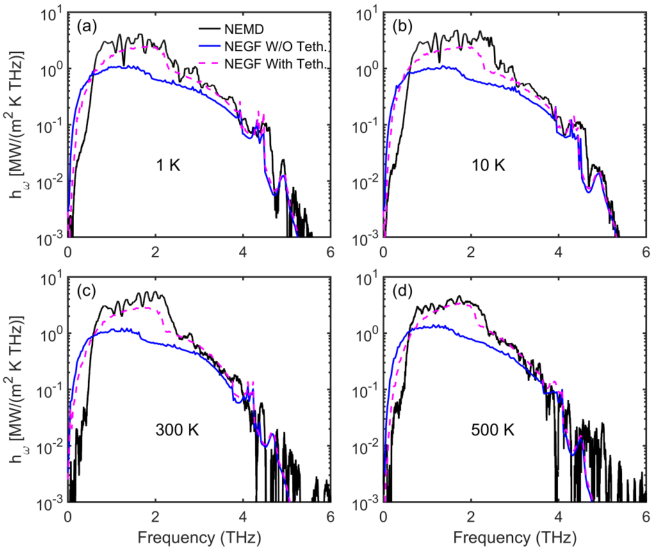

FIG. 6. Spectral thermal conductance of Au-Au nanogap with $d = 3.94$ Å at different temperatures: (a) 1 K, (b) 10 K, (c) 300 K, and (d) 500 K. The black solid line represents the NEMD (nonequilibrium molecular dynamics) result, whereas the blue solid line and magenta dashed line represent the phonon NEGF (nonequilibrium Green's function) results without and with tethering of the surface atomic layers adjacent to the nanogap, respectively.

and harmonic phonon NEGF. We consider small Au-Au and Cu-Cu nanogaps with relaxed gap sizes of 3.94 and 3.45 Å, respectively. In the Au nanogap, four system temperatures of 1, 10, 300, and 500 K are considered, whereas in the Cu nanogap only the first three temperatures are considered. Note the classical statistics are considered in both NEMD and NEGF [via Eq. (7)], and the system temperature is varied to tune the strength of the lattice anharmonicity. In NEMD simulations, the temperature differences of ±0.5, ±5, ±50, and ±50 K are adopted at the four system temperatures, respectively. The thermal expansion effect on the nanogap structure is shown to be very small by optimizing the lattice constant through the *NPT* ensemble at each temperature. For instance, in the Au case, the lattice constants at the four temperatures are 4.0571, 4.0571, 4.0593, and 4.0611 Å, respectively, whereas the relaxed nanogap sizes are 3.9455, 3.9284, 3.9429, and 3.9489 Å, respectively.

The spectral thermal conductances of Au-Au nanogaps computed at different temperatures are shown in Fig. 6. The NEGF spectral conductance with tethering correction is closer to the NEMD one at low temperatures (1 and 10 K) in Figs. 6(a) and 6(b) compared to the situation at 300 K in Fig. 6(c). This can be understood as the amplitude of atomic displacement is reduced with decreasing temperature such that the lattice vibration amplitude is small showing weaker anharmonicity. The ratio of thermal conductance by NEGF over that by NEMD is thus larger at 1 K than those at 10 and 300 K, as shown in Fig. 8(a). The NEMD thermal conductance is higher than the NEGF one (ratio <1), as consistent with the trend of spectral thermal conductances. However, the complex interplay between tethering and anharmonicity makes the underlying mechanism still a bit elusive, which requires further study. As the temperature increases to 500 K, the enhanced anharmonic phonon scattering will decrease a bit the heat transport in NEMD, such that the ratio of thermal conductances increases again. Note that the apparent agreement between NEMD spectral conductance and the NEGF one with tethering correction in Fig. 6(d) is due to the consideration of only harmonic force terms in the SHC decomposition in Eq. (3). As shown in Fig. 8(a), the thermal conductance obtained by NEGF is still around 20% lower than that obtained by the direct NEMD calculation at 500 K. The latter (namely, $6.41\,\mathrm{MW/m^2\,K}$) is slightly larger than the thermal conductance ($6.06\,\mathrm{MW/m^2\,K}$) obtained by integrating the SHC from NEMD.

The results for the Cu-Cu nanogaps are similar, as shown in Figs. 7 and 8(b). As Cu is less anharmonic than Au, the spectral thermal conductance predicted by NEGF with tethering correction at lower temperatures (1 and 10 K) is even closer to the NEMD result, as illustrated in Figs. 7(a) and 7(b). This is also reflected in the slightly larger ratio of thermal conductance by NEGF over that by NEMD as seen in Fig. 8(b). In summary, the effect of anharmonicity is moderate in heat transport across Au-Au and Cu-Cu nanogaps. The difference between the anharmonic and harmonic approaches is

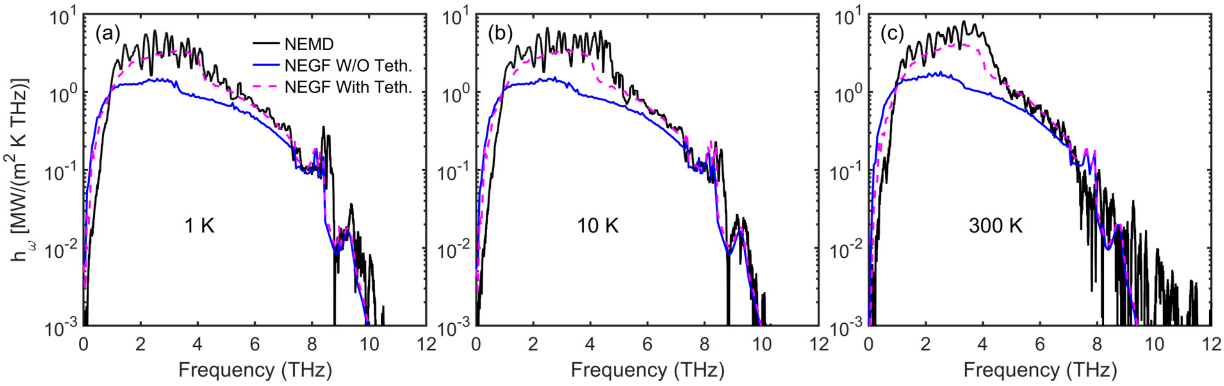

FIG. 7. Spectral thermal conductance of Cu-Cu nanogap with $d = 3.45$ Å at different temperatures: (a) 1 K, (b) 10 K, and (c) 300 K. The black solid line represents the NEMD (nonequilibrium molecular dynamics) result, whereas the blue solid line and magenta dashed line represent the phonon NEGF (nonequilibrium Green's function) results without and with tethering of the surface atomic layers adjacent to the nanogap, respectively.

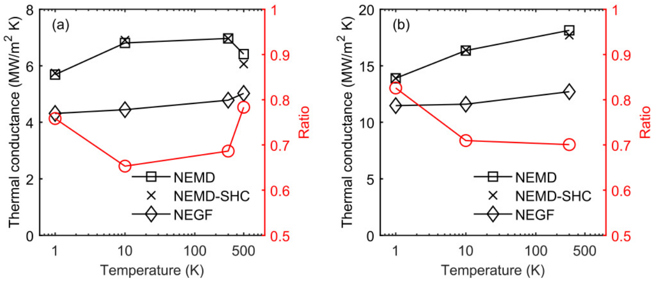

FIG. 8. Temperature-dependent thermal conductance of nanogaps: (a) Au-Au gap with $d = 3.94$ Å, (b) Cu-Cu gap with $d = 3.45$ Å. The squares and diamonds with lines denote the direct NEMD result and NEGF result with tethering, respectively, whereas the circles with line represent the ratio of the thermal conductance by NEGF over that by direct NEMD. The cross symbols represent the thermal conductance by integrating the SHC from NEMD.

around 20%–30% in the studied temperature range. For larger nanogaps, the anharmonic effect is weaker as inferred from the small difference between the NEMD and NEGF thermal conductances in Fig. 2.

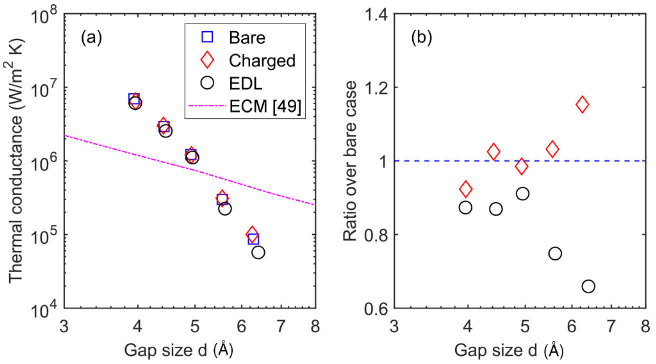

FIG. 9. Electrostatic effect on thermal conductance of Au-Au gap via direct NEMD at room temperature (300 K): (a) thermal conductance; (b) ratio of thermal conductance over bare case. The squares denote the result of bare nanogaps; the diamonds denote the result of nanogaps with uniformly charged surfaces under a constant voltage of 600 mV, corresponding to the experimental setup of Kloppstech *et al.* [12]; and the circles denote the result of nanogaps with electrical double layer (EDL) at the surfaces; the dash-dotted line represents the result of electrostatic phonon heat transfer across nanogaps with EDL based on the elastic continuum model (ECM) in Ref. [49].

C. Effect of electrostatics

In the experimental measurements of the thermal conductance of nanogaps [12,13], a small bias voltage (V) is applied on the system for monitoring the tunneling current of electrons. Under the bias voltage, there will be induced surface charges which produce long-range Coulomb force. The Coulomb force may promote phonon tunneling through enhancing the atomic interactions across the nanogap. Here we explore this electrostatic effect by putting uniform charges with opposite signs at adjacent surfaces of the Au-Au nanogap at 300 K in the NEMD simulation. We follow the method to calculate the surface charge density in the elastic continuum model [25,26]. The surface charge is computed by $q_e = CV$, where the capacitance of the parallel plate-plate configuration is defined as $C = \varepsilon_0 A_c/d$, with ε_0 the vacuum permittivity. The capacitance and surface charge density are calculated based on the relaxed gap size ($d_{\text{relax, bare}}$) as in Table I, whereas a voltage of 600 mV is adopted from the experimental report [12]. We reoptimize the nanogap configuration with surface charges under the *NPT* ensemble and obtain a new relaxed gap size ($d_{\text{relax, charged}}$). In principle, the surface charge density has to be recalculated based on $d_{\text{relax, charged}}$ and the optimization is redone through a self-consistent iterative procedure. However, $d_{\text{relax, charged}}$ after the first iteration is quite close to $d_{\text{relax,bare}}$, as summarized in Table III for the different cases. Thus we adopt the nanogap configuration after the first iteration for further simulation and analysis.

The thermal conductances of the bare and charged Au-Au nanogaps are compared in Fig. 9(a), which shows a very small difference (except the 6.28 Å nanogap) as quantified in Fig. 9(b). The results of large ($\geqslant 7.53$ Å) relaxed nanogaps are no longer shown as the thermal conductance is too low to obtain statistically meaningful heat current in NEMD even in the presence of surface charges. The spectral thermal conductances of three typical nanogaps are compared in Fig. 10 between the bare and charged cases. Although there seems to be minor change of the heat current spectrum across the 6.28 Å nanogap induced by the surface charges, no significant effect is visible in the overall thermal conductance. The present atomistic modeling result is consistent with that by the elastic continuum model [25,26] which shows negligible electrostatic effect on phonon heat transfer across the Au-Au nanogap under a bias voltage of 1 V. However, our conclusion is different from that of a recent 1D harmonic

TABLE III. Initial and relaxed Au-Au nanogap configurations under the corresponding tethering without (bare) or with (charged) a bias voltage of 600 mV.

d_{init} (Å)	$d_{\text{relax,bare}}$ (Å)	Surface charge (e)	Surface charge per atom (e)	Surface charge density (C/m^2)	$d_{\text{relax,charged}}$ (Å)
4.5	3.94	3.56	6.96×10^{-3}	1.35×10^{-2}	3.97
5.0	4.43	3.17	6.19×10^{-3}	1.20×10^{-2}	4.42
5.5	4.92	2.86	5.58×10^{-3}	1.08×10^{-2}	4.93
6.0	5.56	2.53	4.93×10^{-3}	9.55×10^{-3}	5.56
7.0	6.28	2.24	4.37×10^{-3}	8.46×10^{-3}	6.25
8.0	7.52	1.87	3.65×10^{-3}	7.06×10^{-3}	7.53

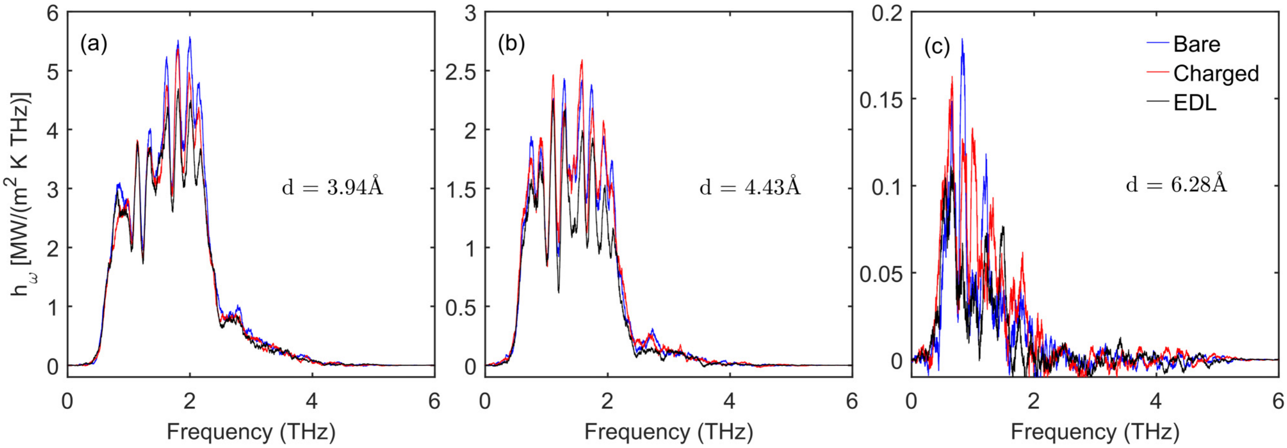

FIG. 10. Electrostatic effect on spectral thermal conductance of Au-Au gap via molecular dynamics at room temperature (300 K): (a) $d = 3.94$ Å, (b) $d = 4.43$ Å, and (c) $d = 6.28$ Å. The blue solid lines denote the results of bare nanogaps; the red solid lines denote the results of nanogaps with uniformly charged surfaces under a constant voltage of 600 mV, corresponding to the experimental setup of Kloppstech *et al.* [12]; and the black lines denote the results of nanogaps with electrical double layer (EDL) at the surfaces. The relaxed gap sizes of the charged nanogaps are 3.97, 4.42, and 6.25 Å, respectively; the relaxed gap sizes of the nanogaps with EDL are 3.96, 4.46, and 6.40 Å, respectively.

phonon NEGF modeling of the Au-Au nanogap [17], which shows large enhancement of the phonon thermal conductance by the bias voltage. The difference is mainly caused by the different treatments of the effect of electrostatic interaction. In Ref. [17], an additional static surface charge was assumed on the sample surface following a previous experimental report on a metal-dielectric tip-surface system [48]. Also the formula of total electrostatic force on the tip from both the dielectric surface and the metal electrode in Ref. [48] was adapted for the Coulombic interaction between the tip and surface [17]. Regarding the metal-metal tip-surface system considered here, we do not find clear evidence to assume an additional static surface charge on a metal surface as on a dielectric surface. Instead, we only consider the induced capacitive charges on the surfaces of the Au-Au nanogap by the bias voltage.

Another possible electrostatic effect comes from the electrical double layer (EDL) at the metal surface even in the absence of bias voltage, as discussed in a very recent work [49] based on an elastic continuum model. The EDL at the metal surface results from the redistribution of the electron density due to the "spill-out" of electrons into vacuum, which induces a negatively charged surface atomic layer and a positively charged uncompensated subsurface atomic layer [49–51]. We investigate this effect via NEMD simulation by putting opposite charges on the two atomic layers near each surface of the Au-Au nanogap. The layer charge density is estimated as [49] $\sigma = \varepsilon_0 \Delta\varphi / e d_0$, with d_0 the interlayer separation, e the elementary charge, and $\Delta\varphi = W_f + \bar{\mu}$ the potential step due to EDL, where W_f and $\bar{\mu}$ are the work function and bulk chemical potential of the contact metal, respectively. As shown in Figs. 9(a) and 9(b), the EDL has a stronger impact on the phonon heat transport across the nanogap compared to the electrostatic effect of the small bias voltage. This is also illustrated in Fig. 10, where a noticeable reduction of spectral thermal conductance is seen in the moderate-frequency (~1–2 THz) range in the presence of EDL. The main underlying mechanism includes (i) the Columbic interaction between the two atomic layers in the EDL alters the lattice vibration near the surface; (ii) the attraction of the negatively charged surface atomic layer by the positively charged subsurface atomic layer reduces a bit the relaxation of the nanogap, as evidenced by the slightly larger ($<1\%$ for small nanogaps, and $<2\%$ for the largest considered nanogap) gap size. Nevertheless, the EDL effect by the present atomistic modeling is generally small in contrast to the dominant electrostatic phonon heat transfer induced by EDL based on the continuum model [49] as included in Fig. 9(a). Note the phonon thermal conductance due to the van der Waals interaction predicted by the continuum model is much smaller as shown in Fig. 3(a). The cause of the difference between atomistic and continuum models deserves further study as discussed in Sec. III A.

D. Discussions

One of the motivations of this work was to explain the experimental thermal conductance of the nanogap in the extremely near-field regime by the phonon transport channel. Although our atomic simulation results are consistent with the experiment of Cui *et al.* [13], they are not able to reproduce the giant experimental conductance of Kloppstech *et al.* [12] in both the magnitude and the decaying slope as discussed in Sec. III A. There are more recent unpublished experimental data included in Ref. [22] for comparison to the theoretical modeling result. However, the measured gap thermal conductance shows a similar trend of slow decay with increasing gap size, which could not be well explained even considering the effect of bias voltage on the electronic tunneling channel [22]. We have also tried to model the phonon heat transport by NEGF with first-principles calculation of interatomic forces across the nanogap, which are, however, comparable to or even smaller than the residual force in structure relaxation for stable gaps larger than ~5 Å. Thus we could not obtain a reliable first- principles modeling result. As all the possible channels (phonons, electrons, photons) have been considered, the disagreement is most probably due to the different conditions between the simulation and the experiment. Clean nanogaps with ideal surface conditions are modeled in the simulation. In contrast, there may be unknown contaminations from the sample fabrication and preparation procedure in experiment, as indicated by the cleaning process dependent apparent barrier heights and thermal conductances [13]. As no tunneling current was observed beyond 1 nm gap size [12,13], the contamination is electrically insulating and is possibly organic molecules. Such organic molecules would bridge the tip and surface, and contribute to a new heat transport channel across the nanogap. A gradual decrease of the thermal conductance has been observed due to the breaking of some molecular junctions when the tip is retracted from the surface within a few nanometers [52]. This physical picture seems to be a possible explanation for the slow decay of thermal conductance versus gap size observed in the experiment of Kloppstech *et al.* [12]. To exclude the effect from contamination and achieve a more definite understanding of the underlying physics, further experimental investigation of the extremely near-field heat transport is pending in the future.

IV. CONCLUSIONS

In summary, we investigate the phonon heat transport across metallic nanogaps by combining molecular dynamics simulation and the three-dimensional harmonic phonon nonequilibrium Green's function method. The tip-surface phonon thermal conductance decays rapidly with the gap size ($\tilde{d}$) through a power law of $\tilde{d}^{-7.6}$, and the phonon tunneling is a significant heat transport channel below the gap size of 1 nm. The effect of lattice anharmonicity on phonon heat transport across the nanogap amounts to within ~20%–30% of the thermal conductance depending on gap size, whereas the impact of small bias voltage used in experimental measurement is found to be weak. Our atomistic simulation is consistent with the experiment by Cui *et al.* [13] while it is not able to explain the giant heat transfer in the experiment by Kloppstech *et al.* [12] probably due to contaminations. The present atomistic simulation framework contributes to a more pertinent modeling of the phonon transport channel and hitherto detailed information of the heat current spectrum across nanogaps. This work thus promotes deeper understanding and a future perspective of heat transport in the extremely near-field regime.

ACKNOWLEDGMENTS

This work has been supported by the ANR project NearHeat (LCF Orsay and iLM Villeurbanne). This research used the computational resources of Raptor of iLM at Université Claude Bernard Lyon 1, the PSMN clusters at ENS de Lyon, and the Oakforest-PACs supercomputer system at The University of Tokyo. The authors appreciate helpful discussions with Dr. R. Messina, Dr. P. Ben-Abdallah, and Dr. M. Gómez Viloria from Université Paris-Saclay, Dr. S. Volz and Dr. Z. Zhang from The University of Tokyo, and Dr. A. Kyritsakis from the University of Tartu.

APPENDIX A: COMPARISON OF LENNARD-JONES POTENTIAL AND GRIMME'S DISPERSION CORRECTION

To make sure that the Lennard-Jones potential captures the long-range dispersion force between metallic atoms, we compare to the Grimme's density functional dispersion correction (DFT-D3) [36]:

$$E_{\mathrm{disp}} = -\frac{C_6}{r^6} f_{d,6}(r), \tag{A1}$$

where the C_6 coefficient is 342.3526 a.u. (atomic unit) for gold, and the damping function is defined as

$$f_{d,6}(r) = \frac{1}{1 + 6[r/(s_{r,6}R_0)]^{-14}}. \tag{A2}$$

The atom pairwise cutoff radius for gold is $R_0 = 3.26$ Å, and the scaling factor $s_{r,6} = 1.532$ based on the PW6B95 functional is adopted due to its small mean absolute deviation [36]. The C_8 term in DFT-D3 is not considered here as it is more short ranged. The dispersion correction in Eq. (A1) is shown in Fig. 11 together with the Lennard-Jones potential used in the present work. The long-range attractive interaction term in the Lennard-Jones potential has the same trend as the dispersion correction, and is negligibly small beyond 12 Å used as the cutoff radius in MD simulation.

APPENDIX B: DERIVATION OF PHONON NEGF FORMALISM WITH EXTERNAL FORCE

Here we present a derivation of 1D phonon NEGF formalism with external tethering force, following the basic idea in classical works [30,53]. In the harmonic approximation, the lattice dynamic equation of atoms under an external harmonic spring is

$$m_p \frac{d^2 u_p}{dt^2} = -\sum_q k_{pq} u_q - k_{\mathrm{spring}} u_p, \tag{B1}$$

where u_p, u_q denotes the vibrational degrees of freedom (i.e., atomic displacements), with m_p the atomic mass associated with u_p, $k_{pq} = \partial^2 \Phi / \partial u_p \partial u_q$ is the second-order force constant with Φ the interatomic potential here, and k_{spring} is the spring constant of the tethering spring.

Owing to the lack of translational lattice symmetry in the studied nanosystem by 1D phonon NEGF, the normal mode solution of Eq. (B1) with respect to time t has the following form [53]:

$$u_p = \frac{1}{\sqrt{m_p}} \phi_p \exp(-i\omega t), \tag{B2}$$

with ω, ϕ_p the frequency and amplitude of the vibrational degree of freedom, respectively. Putting the solution of Eq. (B2) into the lattice dynamic equation in Eq. (B1), we obtain the dynamic equation in the frequency domain as

$$\left(\omega^2 - \frac{k_{\mathrm{spring}}}{m_p}\right)\phi_p - \sum_q \Phi_{pq}\phi_q = 0, \tag{B3}$$

where the components of the dynamic matrix are defined as $\Phi_{pq} \equiv k_{pq}/\sqrt{M_p M_q}$. Equation (B3) can be rewritten into the

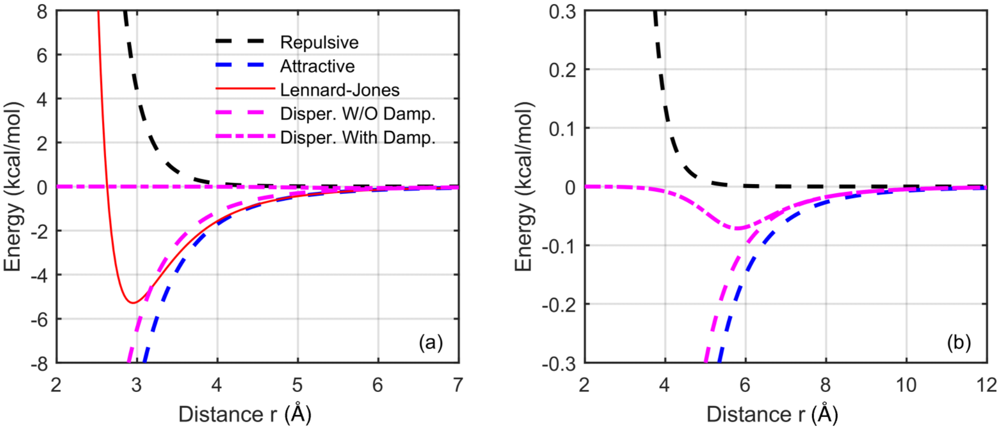

FIG. 11. Comparison of Lennard-Jones potential and Grimme's DFT-D3 dispersion correction for gold.

matrix notation as

$$\left[\left(\omega^2 - \frac{k_{\mathrm{spring}}}{m_p}\right)\mathbf{I} - \mathbf{\Phi}\right]\phi = 0, \tag{B4}$$

where $\mathbf{I}$ and $\mathbf{\Phi}$ are, respectively, the unity matrix and dynamic matrix of dimension $N_p \times N_p$, whereas ϕ is a $N_p \times 1$ column vector, with N_p the total number of vibrational degrees of freedom of the system. The retarded Green's function of the device region in the form of Eqs. (4) and (8) can be derived straightforwardly from Eq. (B4) by splitting the system into two contact regions and a device region [53]. For the considered case with only tethering force along the transport direction (x direction) in the present work, Eq. (B4) is reduced to

$$\left[\omega^2\mathbf{I} - \frac{k_{\mathrm{spring}}}{m_p}\mathbf{I}_1 - \mathbf{\Phi}\right]\phi = 0, \tag{B5}$$

with the diagonal matrix $\mathbf{I}_1$ defined as

$$\mathbf{I}_1 = \begin{bmatrix} 1 & & & & & & \mathbf{0} \\ & 0 & & & & & \\ & & 0 & & & & \\ & & & 1 & & & \\ & & & & 0 & & \\ & & & & & 0 & \\ \mathbf{0} & & & & & & \ddots \end{bmatrix}. \tag{B6}$$

Finally, the formulation of 3D phonon NEGF used in the present work [i.e., Eq. (8)] is obtained by introducing the Fourier's representation into the 1D formulation derived here along the transverse direction.

APPENDIX C: ELECTRONIC TUNNELING HEAT CURRENT ACROSS VACUUM NANOGAPS

Here we explain the heat current associated with the electronic tunneling across a vacuum nanogap. Consider the two identical metallic contacts at temperatures T_1, T_2 and chemical potentials μ_1, μ_2, respectively. In the absence of a bias voltage, $\mu_1 = \mu_2 = E_f$, whereas in the presence of a bias voltage (V), $\mu_1 = E_f$ and $\mu_2 = E_f – eV$, with E_f the Fermi level of the metal and e the elementary charge.

The heat current leaving contact 1 associated with the electronic tunneling can be written in the form of the Landauer formula [54,55]:

$$Q_{e1} = \frac{m}{2\pi^2\hbar^3}\int_0^\infty dE_x \int_0^\infty dE_r (E - \mu_1)[f_1(E) - f_2(E)]\tau(E_x). \tag{C1}$$

Equation (C1) can be derived for the 3D plate-plate configuration from

$$Q_{e1} = 2\int_0^\infty \int_{-\infty}^\infty \int_{-\infty}^\infty v_x(E - \mu_1)[f_1(E) - f_2(E)]\tau(E_x)\frac{\mathrm{d}k_y\mathrm{d}k_z\mathrm{d}k_x}{(2\pi)^3}, \tag{C2}$$

where v_x, E_x, and $\tau(E_x)$ are the velocity, energy, and transmission probability of electrons along the transport direction, respectively. The factor "2" expresses the spin degeneracy. The Fermi-Dirac distributions in contact 1(2) are expressed as $f_{1(2)}(E) = \{\exp[(E - \mu_{1(2)})/k_B T_{1(2)}] + 1\}^{-1}$. The free electron gas model has been assumed for metals [56]:

$$E = E_x + E_r = \frac{\hbar^2 k_x^2}{2m} + \frac{\hbar^2 k_r^2}{2m} = \frac{1}{2}mv_x^2 + \frac{1}{2}mv_r^2, \tag{C3}$$

where the cylindrical coordinate system is introduced for treating the periodic transverse direction: $k_r^2 = k_y^2 + k_z^2$, $v_r^2 = v_y^2 + v_z^2$, with v_y, v_z the velocities along the y and z directions (v_r being the overall velocity along the radial direction). The integration in

Eq. (C1) can be divided into two parts:

$$Q_{e1} = \frac{m}{2\pi^2\hbar^3}\int_0^\infty dE_x(E_x-\mu_1)\tau(E_x)\int_0^\infty dE_r[f_1(E)-f_2(E)] + \frac{m}{2\pi^2\hbar^3}\int_0^\infty dE_x\tau(E_x)\int_0^\infty dE_r[f_1(E)-f_2(E)]E_r. \tag{C4}$$

Accomplishing the integration over E_r in the first part of Eq. (C4), we obtain

$$Q_{e1} = \int_0^\infty (E_x-\mu_1)\tau(E_x)[N_1(E_x)-N_2(E_x)]dE_x + \int_0^\infty dE_x\tau(E_x)\frac{m}{2\pi^2\hbar^3}\int_0^\infty dE_r[f_1(E)-f_2(E)]E_r, \tag{C5}$$

where $N_{1(2)}(E_x)$ denote the number of electrons in contact 1(2) per unit area, per unit time, per unit energy interval along the transport direction [57]:

$$N_{1(2)}(E_x) = \frac{mk_BT_{1(2)}}{2\pi^2\hbar^3}\ln\left[\exp\left(-\frac{E_x-\mu_{1(2)}}{k_BT_{1(2)}}\right)+1\right]. \tag{C6}$$

The transmission probability of electrons across the vacuum nanogap is calculated based on the WKB (Wentzel-Kramers-Brillouin) approximation [56]:

$$\tau(E_x) = \exp\left[-\frac{\sqrt{8m_e}}{\hbar}\int_{x_1}^{x_2}\sqrt{W(x)-E_x}dx\right], \tag{C7}$$

where m_e is the electron mass; $W(x)$ is the potential barrier profile in the nanogap; and x_1, x_2 are zeros of $W(x)-E_x$. We include the effect of image charge in the potential barrier profile: $W(x) = W_{id}(x) + W_{ic}(x)$, where the ideal linear profile and the image charge correction are expressed, respectively, as [17,57,58]

$$W_{id}(x) = \mu_1 + W_f - \frac{x}{d}eV, \tag{C8}$$

$$W_{ic}(x) = \frac{e^2}{16\pi\varepsilon_0 d}\left[-2\psi(1) + \psi\left(\frac{x}{d}\right) + \psi\left(1-\frac{x}{d}\right)\right]. \tag{C9}$$

In Eq. (C8), W_f is the work function of the metal. In Eq. (C9), ε_0 is the vacuum permittivity, and $\psi(\bar{x})$ is the digamma function.

[1] M. Reina, R. Messina, and P. Ben-Abdallah, Phys. Rev. Lett. **125**, 224302 (2020).

[2] M. Reina, R. Messina, and P. Ben-Abdallah, Phys. Rev. B **104**, L100305 (2021).

[3] L. Olesen, M. Brandbyge, M. R. Sørensen, K. W. Jacobsen, E. Lægsgaard, I. Stensgaard, and F. Besenbacher, Phys. Rev. Lett. **76**, 1485 (1996).

[4] I. Altfeder, A. A. Voevodin, and A. K. Roy, Phys. Rev. Lett. **105**, 166101 (2010).

[5] M. H. Kryder, E. C. Gage, T. W. McDaniel, W. A. Challener, R. E. Rottmayer, G. Ju, Y.-T. Hsia, and M. F. Erden, Proc. IEEE **96**, 1810 (2008).

[6] W. Challener, C. Peng, A. Itagi, D. Karns, W. Peng, Y. Peng, X. Yang, X. Zhu, N. Gokemeijer, and Y.-T. Hsia, Nat. Photonics **3**, 220 (2009).

[7] B. C. Stipe, H. J. Mamin, T. D. Stowe, T. W. Kenny, and D. Rugar, Phys. Rev. Lett. **87**, 096801 (2001).

[8] A. I. Volokitin and B. N. J. Persson, Rev. Mod. Phys. **79**, 1291 (2007).

[9] M. Lee, R. L. C. Vink, C. A. Volkert, and M. Krüger, Phys. Rev. B **104**, 174309 (2021).

[10] S. Y. Mesnyankin, A. G. Vikulov, and D. G. Vikulov, Phys. Usp. **52**, 891 (2009).

[11] Y. Xian, P. Zhang, S. Zhai, P. Yuan, and D. Yang, Appl. Therm. Eng. **130**, 1530 (2018).

[12] K. Kloppstech, N. Könne, S.-A. Biehs, A. W. Rodriguez, L. Worbes, D. Hellmann, and A. Kittel, Nat. Commun. **8**, 14475 (2017).

[13] L. Cui, W. Jeong, V. Fernández-Hurtado, J. Feist, F. J. García-Vidal, J. C. Cuevas, E. Meyhofer, and P. Reddy, Nat. Commun. **8**, 14479 (2017).

[14] S. Xiong, K. Yang, Y. A. Kosevich, Y. Chalopin, R. D'Agosta, P. Cortona, and S. Volz, Phys. Rev. Lett. **112**, 114301 (2014).

[15] A. Jarzembski, T. Tokunaga, J. Crossley, J. Yun, C. Shaskey, R. A. Murdick, I. Park, M. Francoeur, and K. Park, arXiv:1904.09383.

[16] L. Ghaderipoor, M. Mardaani, E. Amooghorban, and H. Rabani, Phys. Rev. E **104**, 034121 (2021).

[17] T. Tokunaga, A. Jarzembski, T. Shiga, K. Park, and M. Francoeur, Phys. Rev. B **104**, 125404 (2021).

[18] T. Tokunaga, M. Arai, K. Kobayashi, W. Hayami, S. Suehara, T. Shiga, K. Park, and M. Francoeur, Phys. Rev. B **105**, 045410 (2022).

[19] M. Prunnila and J. Meltaus, Phys. Rev. Lett. **105**, 125501 (2010).

[20] B. V. Budaev and D. B. Bogy, Appl. Phys. Lett. **99**, 053109 (2011).

[21] J. B. Pendry, K. Sasihithlu, and R. V. Craster, Phys. Rev. B **94**, 075414 (2016).

[22] R. Messina, S.-A. Biehs, T. Ziehm, A. Kittel, and P. Ben-Abdallah, arXiv:1810.02628.

[23] D. P. Sellan, E. S. Landry, K. Sasihithlu, A. Narayanaswamy, A. J. H. McGaughey, and C. H. Amon, Phys. Rev. B **85**, 024118 (2012).

[24] A. Alkurdi, C. Adessi, F. Tabatabaei, S. Li, K. Termentzidis, and S. Merabia, Int. J. Heat Mass Transfer **158**, 119963 (2020).

[25] A. I. Volokitin, JETP Lett. **109**, 749 (2019).
[26] A. Volokitin, J. Phys.: Condens. Matter **32**, 215001 (2020).
[27] W. Chen and G. Nagayama, Int. J. Heat Mass Transfer **176**, 121431 (2021).
[28] S. G. Volz and G. Chen, Phys. Rev. B **61**, 2651 (2000).
[29] S. Merabia and K. Termentzidis, Phys. Rev. B **86**, 094303 (2012).
[30] N. Mingo and L. Yang, Phys. Rev. B **68**, 245406 (2003).
[31] T. Yamamoto and K. Watanabe, Phys. Rev. Lett. **96**, 255503 (2006).
[32] Y. Guo, M. Bescond, Z. Zhang, M. Luisier, M. Nomura, and S. Volz, Phys. Rev. B **102**, 195412 (2020).
[33] A. P. Thompson, H. M. Aktulga, R. Berger, D. S. Bolintineanu, W. M. Brown, P. S. Crozier, P. J. in't Veld, A. Kohlmeyer, S. G. Moore, and T. D. Nguyen, Comput. Phys. Commun. **271**, 108171 (2022).
[34] B. Grabowski, T. Hickel, and J. Neugebauer, Phys. Rev. B **76**, 024309 (2007).
[35] H. Heinz, R. Vaia, B. Farmer, and R. Naik, J. Phys. Chem. C **112**, 17281 (2008).
[36] S. Grimme, J. Antony, S. Ehrlich, and H. Krieg, J. Chem. Phys. **132**, 154104 (2010).
[37] K. Sääskilahti, J. Oksanen, J. Tulkki, and S. Volz, Phys. Rev. B **90**, 134312 (2014).
[38] K. Sääskilahti, J. Oksanen, S. Volz, and J. Tulkki, Phys. Rev. B **91**, 115426 (2015).
[39] W. Zhang, T. Fisher, and N. Mingo, J. Heat Transfer **129**, 483 (2007).
[40] Y. Guo, M. Bescond, Z. Zhang, S. Xiong, K. Hirakawa, M. Nomura, and S. Volz, APL Mater. **9**, 091104 (2021).
[41] F. Guinea, C. Tejedor, F. Flores, and E. Louis, Phys. Rev. B **28**, 4397 (1983).
[42] A. Togo and I. Tanaka, Scr. Mater. **108**, 1 (2015).
[43] G. Domingues, S. Volz, K. Joulain, and J.-J. Greffet, Phys. Rev. Lett. **94**, 085901 (2005).
[44] Z. M. Zhang, *Nano/Microscale Heat Transfer* (McGraw-Hill, New York, 2007).
[45] M. A. Ordal, R. J. Bell, R. W. Alexander, L. L. Long, and M. R. Querry, Appl. Opt. **24**, 4493 (1985).
[46] P.-O. Chapuis, S. Volz, C. Henkel, K. Joulain, and J.-J. Greffet, Phys. Rev. B **77**, 035431 (2008).
[47] Y. Guo, Z. Zhang, M. Bescond, S. Xiong, M. Nomura, and S. Volz, Phys. Rev. B **103**, 174306 (2021).
[48] B. D. Terris, J. E. Stern, D. Rugar, and H. J. Mamin, Phys. Rev. Lett. **63**, 2669 (1989).
[49] A. I. Volokitin, Phys. Rev. B **103**, L041403 (2021).
[50] N. Lang and W. Kohn, Phys. Rev. B **3**, 1215 (1971).
[51] A. Volokitin, Appl. Surf. Sci. Adv. **6**, 100160 (2021).
[52] N. Mosso, H. Sadeghi, A. Gemma, S. Sangtarash, U. Drechsler, C. Lambert, and B. Gotsmann, Nano Lett. **19**, 7614 (2019).
[53] W. Zhang, T. Fisher, and N. Mingo, Numer. Heat Transfer, Part B **51**, 333 (2007).
[54] U. Sivan and Y. Imry, Phys. Rev. B **33**, 551 (1986).
[55] J. Xu, K. Läuger, R. Möller, K. Dransfeld, and I. Wilson, Appl. Phys. A **59**, 155 (1994).
[56] J. G. Simmons, J. Appl. Phys. **34**, 1793 (1963).
[57] Y. Hishinuma, T. Geballe, B. Moyzhes, and T. W. Kenny, Appl. Phys. Lett. **78**, 2572 (2001).
[58] I. Bâldea and H. Köppel, Phys. Status Solidi B **249**, 1791 (2012).